Intelligent Computing
A SCIENCE PARTNER JOURNAL

RESEARCH ARTICLE

Freeform Illuminator for Computational Microscopy

Pengming Song[1†], Tianbo Wang[1†], Shaowei Jiang[1], Chengfei Guo[1,2], Ruihai Wang[1], Liming Yang[1], You Zhou[3], and Guoan Zheng[1*]

[1]Department of Biomedical Engineering, University of Connecticut, Storrs, CT 06269, USA. [2]Advanced Optoelectronic Imaging and Device Laboratory, Hangzhou Institute of Technology, Xidian University, Hangzhou 311200, China. [3]School of Electronic Science and Engineering, Nanjing University, Nanjing 210023, China.

*Address correspondence to: guoan.zheng@uconn.edu
†These authors contributed equally to this work.

Citation: Song P, Wang T, Jiang S, Guo C, Wang R, Yang L, Zhou Y, Zheng G. Freeform Illuminator for Computational Microscopy. *Intell. Comput.* 2023;2:Article 0015. https://doi.org/10.34133/icomputing.0015

Submitted 23 August 2022
Accepted 22 December 2022
Published 20 February 2023

Programmable illumination control is essential for many computational microscopy techniques. Conventional light source array is often arranged on a fixed grid of a planar surface for providing programmable sample illumination. Here, we report the development of a freeform illuminator that can be arranged at arbitrary 2-dimensional or 3-dimensional (3D) surface structures for computational microscopy. The freeform illuminator can be designed in a small form factor with a dense light source arrangement in 3D. It can be placed closer to the sample for providing angle-varied illumination with higher optical flux and smaller angular increment. With the freeform illuminators, we develop a calibration process using a low-cost Raspberry-Pi image sensor coated with a monolayer of blood cells. By tracking the positional shift of the blood-cell diffraction patterns at 2 distinct regions of the coded sensor, we can infer the 3D positions of the light source elements in a way similar to the stereo vision reconstruction approach. To demonstrate the applications for computational microscopy, we validate the freeform illuminators for Fourier ptychographic microscopy, 3D tomographic imaging, and on-chip microscopy. We also present a longitudinal study by tracking the growth of live bacterial cultures over a large field of view. The reported freeform illuminators and the related calibration process offer flexibilities and extended scope for imaging innovations in computational microscopy.

Introduction

Illumination engineering is essential for obtaining high-resolution, high-quality images in microscope settings. In a conventional light microscope, an illumination module based on a condenser lens is utilized for providing uniform sample illumination that is free from glare. This illumination module typically consists of a high-numerical-aperture (NA) condenser lens and a condenser diaphragm for controlling the illumination NA. Adjustment of the condenser diaphragm allows one to have different illumination conditions for microscopy imaging. For regular bright-field microscopy, the illumination NA needs to match the detection NA of the objective lens. The size of the condenser diaphragm can be adjusted according to the NA of the objective lens. For dark-field microscopy, the illumination NA needs to exceed the detection NA of the objective lens. An aperture stop can be added to the condenser diaphragm to block the light with low-illumination NA. For oblique illumination microscopy, a small aperture can be placed at an off-axis position of the diaphragm plane to select light waves with a tilted incident angle. In this case, refraction index gradients in the specimen deflect the oblique light wave so that only the zeroth order and one diffracted sideband can recombine at the image plane. This produces a relief-like image having regions displaying shadows and highlights, much like that observed with the differential interference contrast technique [1]. For phase contrast microscopy, a ring aperture can be placed at the diaphragm plane to match the ring-shaped phase plate of the objective lens.

From these examples and others, we can see that different microscopy techniques require vastly different illumination conditions. Instead of using the regular condenser lens module, the use of cost-effective programmable light sources for computational microscopy has received considerable attention in recent years. They have been demonstrated for different imaging applications, including 3D tomographic imaging, resolution improvement beyond the NA limit of the objective lens, differential phase contrast imaging, polarization-sensitive imaging, rapid autofocusing, single-pixel imaging, on-chip microscopy, and more [2–40].

Early demonstrations of programmable light sources include the use of a smartphone screen to provide angle-varied illumination for an on-chip microscopy platform [4,6,13] and the use of multiple fibers for on-chip tomographic imaging [2,3]. In the former case, bio-specimens are directly placed on top of an

image sensor. By illuminating the specimens from different incident angles, the platform records the shadow images without using any lens. Since there is a gap between the specimens and the light-sensitive pixels, angle-varied illumination in this platform leads to subpixel shifts of the acquired shadow images through the projection process. One can then recover the large field-of-view, high-resolution object images using the pixel super-resolution algorithm [41]. In the latter case, different fibers are used to illuminate the sample from different incident angles. By combining holographic reconstruction with tomographic imaging, it can recover the volumetric information of the sample on a chip. Other lensless examples of angle-varied illumination include a real-space ptychographic microscope built with a light-emitting diode (LED) array [27], mask-modulated lensless microscope platforms [18,19,39], and a lensless phase microscope based on multiangle and multiwavelength illumination [33], among others.

For a lens-based system, angle-varied illumination can be implemented by replacing the condenser module with a programmable LED array. One example is Fourier ptychographic microscopy (FPM) [7], where the specimen is illuminated from different incident angles and a low-NA objective lens is used for image acquisition. At each angle, the recorded image corresponds to the information from a circular pupil aperture in the Fourier domain. All captured images can be synthesized in the Fourier domain using an iterative phase retrieval process. A complex-valued, high-resolution object image can then be obtained with both intensity and phase properties. The recovered image also retains the original large field of view set by the low-NA objective lens. Since its first demonstration, FPM has evolved from a simple microscope tool to a general technique for different imaging communities [42]. For example, the FPM concept has been integrated with multislice modeling [12,43] or diffraction tomography [22,28] for 3D microscopy imaging. Other lens-based examples of angle-varied illumination include 3D tomographic imaging [5], differential phase contrast microscopy with an LED array [36], color-coded LED illumination for quantitative phase imaging [17,40], single-pixel imaging [32], and holographic imaging via Kramers–Kronig relations [37,44], among others.

In this work, we report the development of freeform illuminators and the associated calibration process for computational microscopy. Different from the conventional light source array that is arranged on a fixed grid of a planar surface, the freeform illuminator can be arranged at arbitrary 2-dimensional (2D) or 3-dimensional (3D) surface structures. It can be designed in a small form factor with a dense light source arrangement in 3D. Thanks to its small footprint, it can be placed closer to the sample for providing angle-varied illumination with higher optical flux and a smaller angular increment. One key consideration for the freeform illuminator is to calibrate the incident angles or the 3D locations of individual light source elements in the array. To this end, we develop a calibration process using a low-cost image sensor coated with a layer of blood cells. The blood-cell monolayer on the sensor coverglass modulates the incoming light waves and generates a diffraction pattern on the detector plane. By tracking the positional shift of the blood-cell diffraction patterns at 2 distinct regions, we can infer the 3D positions of the light source array. This process is similar to the concept of 3D reconstruction via stereo vision. Once calibrated, the freeform illuminator can be adopted in different computational microscopy techniques. Here, we demonstrate its applications in FPM, 3D tomographic imaging, and on-chip microscopy. We also demonstrate a proof-of-concept longitudinal experiment by tracking the growth of live bacterial cultures over a large field of view. The reported freeform illuminators and the related calibration process offer flexibilities and extended scope for imaging innovations in computational microscopy.

Materials and Methods

Overview of the freeform illumination and its applications

Figure 1A shows the overview of the proposed freeform illuminator and its calibration process. For the design of the freeform illuminator, we can arrange different LED elements on arbitrary 2D or 3D surface structures. The left panel of Fig. 1A shows one freeform illuminator design by placing 3 LED arrays on the surfaces of an inverse triangular pyramid. To recover the light source locations in 3D, we develop a calibration procedure by using a blood-coated image sensor (discussed later). Once the light source locations are recovered, we can integrate the illuminator into different computational microscopy setups for sample illumination.

Figure 1B shows the applications of the proposed illuminator for 3 different computational microscopy approaches, namely, FPM [7], 3D tomographic imaging [5], and on-chip microscopy [4,6,13]. The FPM application is shown in the first row of the panel, where we replace the condenser lens module in a regular light microscope with the freeform illuminator. In this application, we only consider 2D thin sections mounted on microscope slides. The forward imaging model of the FPM modality can be expressed as follows:

$$I_i(x,y) = \left| \mathcal{F}^{-1}\left\{ O\left(k_x - k_{xi}, k_y - k_{yi}\right) \cdot CTF\left(k_x, k_y\right) \right\} \right|^2, \quad (1)$$

where $I_i(x, y)$ is the captured image under the illumination of the ith LED element, $O(k_x, k_y)$ is the object's Fourier spectrum, (k_x, k_y) represent the coordinates in the Fourier space, (k_{xi}, k_{yi}) represent the illumination wavevector of the ith LED element, and $CTF(k_x, k_y)$ is the coherent transfer function of the microscope system. To recover the object spectrum, we adopted the extended ptychographic iterative engine for the iterative reconstruction process [45]. This algorithm estimates the intensity measurement at the detector plane. The difference between the intensity estimation and the actual measurement is then used to update the object spectrum. The recovered Fourier spectrum is then transformed back to the spatial domain, obtaining a high-resolution, large-area object reconstruction with both intensity and phase properties. We note that the incident wavevector of the LED array varies across different regions of the large field of view in FPM. Therefore, we need to recover the 3D positions of the LED elements to infer the wavevectors at different regions of the field of view.The second row of Fig. 1B shows the application for 3D tomographic reconstruction. The acquisition process is similar to that of FPM; i.e., we acquire sample images corresponding to different illumination angles. Different from the single 2D section in FPM, the sample for this application is optically thick and needs to be modeled as multiple layers for volumetric reconstruction. The forward imaging model of this 3D tomographic imaging scheme can be expressed as follows:

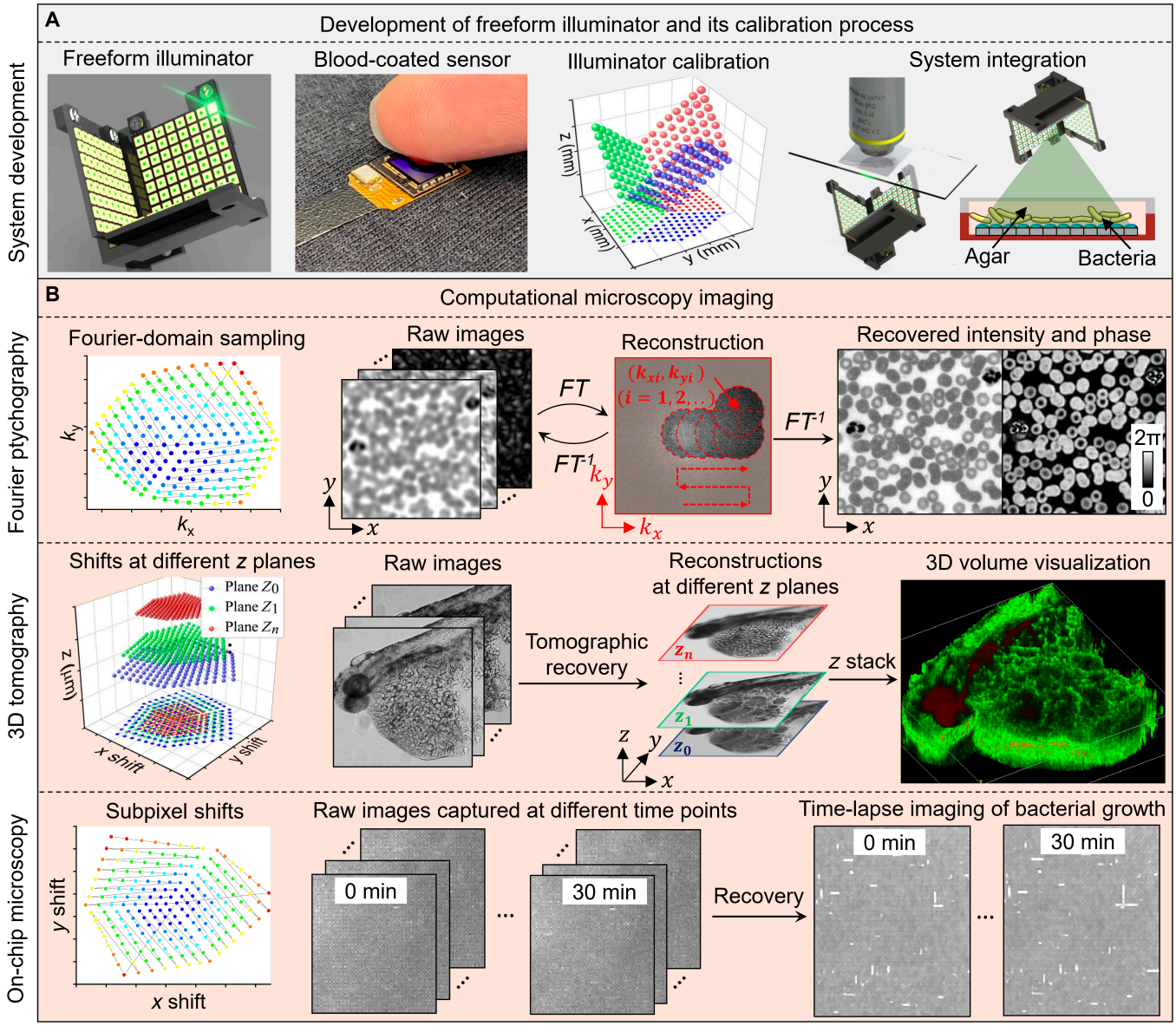

Fig. 1. Overview of the proposed freeform illuminator for computational microscopy. (A) The development of the illuminator and its calibration process. We use a blood-coated image sensor to infer the 3D light source positions. (B) The use of the freeform illuminators for FPM (the first row), 3D tomographic imaging (the middle row), and on-chip microscopy (the bottom row).

$$I_i(x,y) = \sum_j \left| O_{z_j}\left(x - \tan\left(\theta_{xi}\right)\cdot z_j, y - \tan\left(\theta_{yi}\right)\cdot z_j\right)\right|^2 \quad (2)$$

where $I_i(x,y)$ is the captured image under the illumination of the ith LED element, $O_{zj}(x,y)$ represents the object section at the axial depth $z_j = \Delta z \bullet j$, and $(\theta_{xi}, \theta_{yi})$ are the illumination angles of the ith LED element along the x and y directions. The captured image represents a summation of the projected object sections at different depths (the summation over index "j"). We adopted the filtered back projection approach to recover these sections in this work.

The third row of Fig. 1B shows the application for pixel super-resolution on-chip microscopy. We note that the term "super-resolution" here refers to a resolution better than the pixel size, not a resolution better than the diffraction limit. Different from FPM and 3D tomographic imaging, we do not use any lens in this application. The coverglass of the image sensor (MT9P031, On Semiconductor, 2.2 μm pixel size) is removed and the samples are directly placed on top of the pixel array. The forward imaging model of the pixel super-resolution on-chip microscopy approach can be expressed as follows:

$$I_i(x,y) = \text{downsample}\left\{\left|O\left(x - tan\left(\theta_{xi}\right)\cdot d, y - tan\left(\theta_{yi}\right)\cdot d\right)\right|^2\right\}, \quad (3)$$

where $I_i(x,y)$ is the captured image under the illumination of the ith LED element, $O(x,y)$ represents the object, d presents the thickness of the passivation layer on top of the pixel array, and $(\theta_{xi}, \theta_{yi})$ represent the illumination angles of the ith LED element along the x and y directions. Since no lens is used for image magnification, the resolution of the captured images is limited by the pixel size of the detector. Based on the recovered incident angles of the illuminator, these captured images can

be synthesized into one high-resolution, high-contrast image using the pixel super-resolution algorithm [41]. As we will discuss in the next section, a proof-of-concept experiment is performed to track the growth of live bacterial cultures over a large field of view. With this platform, we can start to transit Petri-dish-based experiments from the traditional labor-intensive process to an automated and streamlined process. We also note that it is possible to integrate this lensless microscopy modality with 3D tomography for imaging 3D samples on a chip [33]. In addition to the 3 imaging applications, the freeform illuminator can also be adopted in other microscopy modalities. For example, it can be used in spatial domain coded ptychography for high-throughput imaging without involving mechanical scanning [46]. Similarly, it can be used to generate phase contrast and perform multiwavelength phase retrieval [11,33].

Calibration of freeform illuminator using a blood-coated sensor

While the freeform illuminator adds flexibility to system design, it is important to recover the 3D locations of the light sources for subsequent microscopy applications. We have developed a calibration process using a low-cost Raspberry-Pi camera shown in Fig. 2 (Sony IMX 519). As shown in Fig. 2A, we followed the blood sugar test protocol to obtain a drop of blood from a finger prick. In Fig. 2B, we smeared the blood on top of the coverglass of the image sensor and fixed it with ethyl alcohol for morphology preservation. The blood-coated sensor was then mounted on a microscope slide and placed in the lens-based imaging system, as shown in Fig. 2C and D. To align the blood-coated sensor with respect to the microscope camera, we first marked the boundary and the center of the blood-coated sensor on a blank glass slide. We then imaged this slide using the microscope camera. By adjusting the position of the marked slide using the microscope stage, we can match the center of the blood-coated sensor to the center of the microscope camera. For the lensless on-chip microscopy system, the coverglass of the image sensor has been removed. Therefore, we can make a blood smear on a coverslip instead and place it on top of the sensor for illuminator calibration.

The smearing process in Fig. 2 forms a dense monolayer of blood cells on the sensor. The light interaction with this layer can be modeled using a simple multiplication process [46], allowing the tracking of translational shifts of the diffraction pattern under different incident angles. In contrast, light interaction with conventional disordered media or diffusers cannot be modeled using a simple multiplication process [47]. Compared with the fabrication process of metasurfaces and disorder-engineered surfaces, smearing the blood on the sensor requires no sophisticated tool [48]. It can be performed in ~5 min with ~US$0 cost. However, we also note that an improper procedure of drawing blood would spread bloodborne diseases. Alternatives include blood phantoms, low-risk fish blood from supermarkets, and other small particles that can be made into a thin but dense monolayer on the sensor's coverglass. To determine the distance between the blood-coated layer and the pixel array, we capture a reference image of the blood-coated layer under a normal incident plane wave. We then digitally propagate back to different z positions and pick the best focal plane via visual inspection. We note that, for a specific detector, this distance remains the same for all experiments.

Figure 3 shows the proposed calibration procedure for the freeform illuminator. We first capture a reference image I_{ref} using a normal-incidence plane wave in Fig. 3A. We then place the blood-coated sensor in the imaging setup where the freeform illuminator is used as the light source. A sequence of images I_j ($j = 1, 2, 3\ldots$) is captured by turning on different light elements on the illuminator. With I_{ref} and I_j, we select 2 distinct 512-by-512 pixels tiles in Fig. 3A and B. These regions are denoted as I_j^l, I_j^r, I_{ref}^l, and I_{ref}^r. The superscripts "l" and "r" in the notation represent "left" and "right", respectively. For the jth element of the freeform illuminator, we can calculate the positional shifts of the blood-cell projection pattern at these 2 distinct regions as follows:

$$\left(\Delta x_j^l, \Delta y_j^l\right) = \arg\max_{(x,y)} \left\{ I_{ref}^l \star I_j^l \right\}(x,y) \tag{4}$$

$$\left(\Delta x_j^r, \Delta y_j^r\right) = \arg\max_{(x,y)} \left\{ I_{ref}^r \star I_j^r \right\}(x,y), \tag{5}$$

where "$\star$" denotes the cross-correlation operation, $\left(\Delta x_j^l, \Delta y_j^l\right)$ represents the positional shift of the left region corresponding

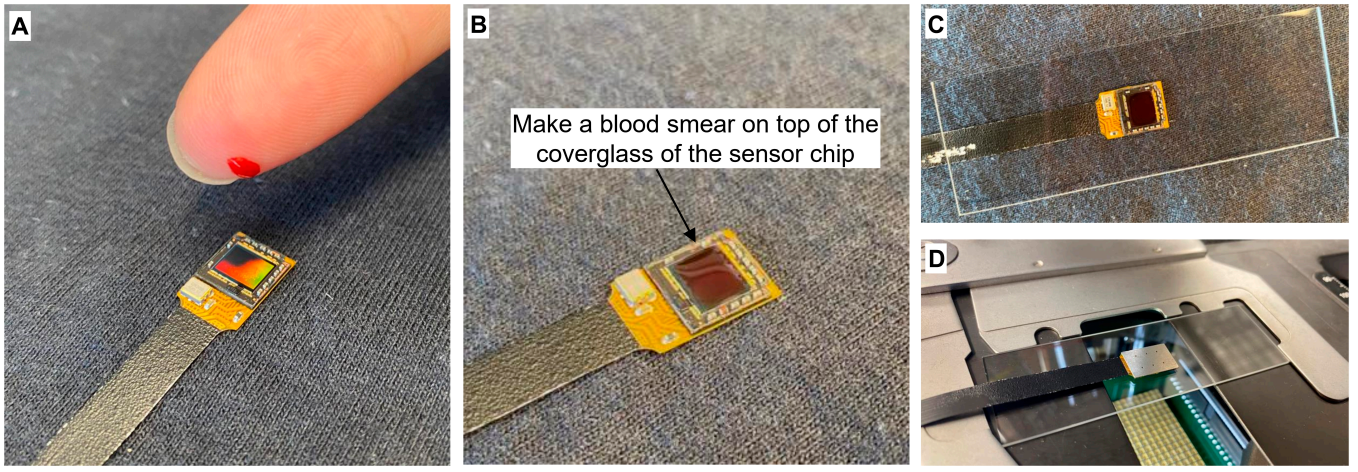

Fig. 2. Blood-coated image sensor for calibration of the freeform illuminator. (A) A drop of blood is obtained from a finger prick. (B) The blood is smeared on top of the sensor's coverglass and fixed with ethyl alcohol. (C) The blood-coated sensor is mounted on a microscope slide. (D) The slide is placed in the microscope system for the calibration process.

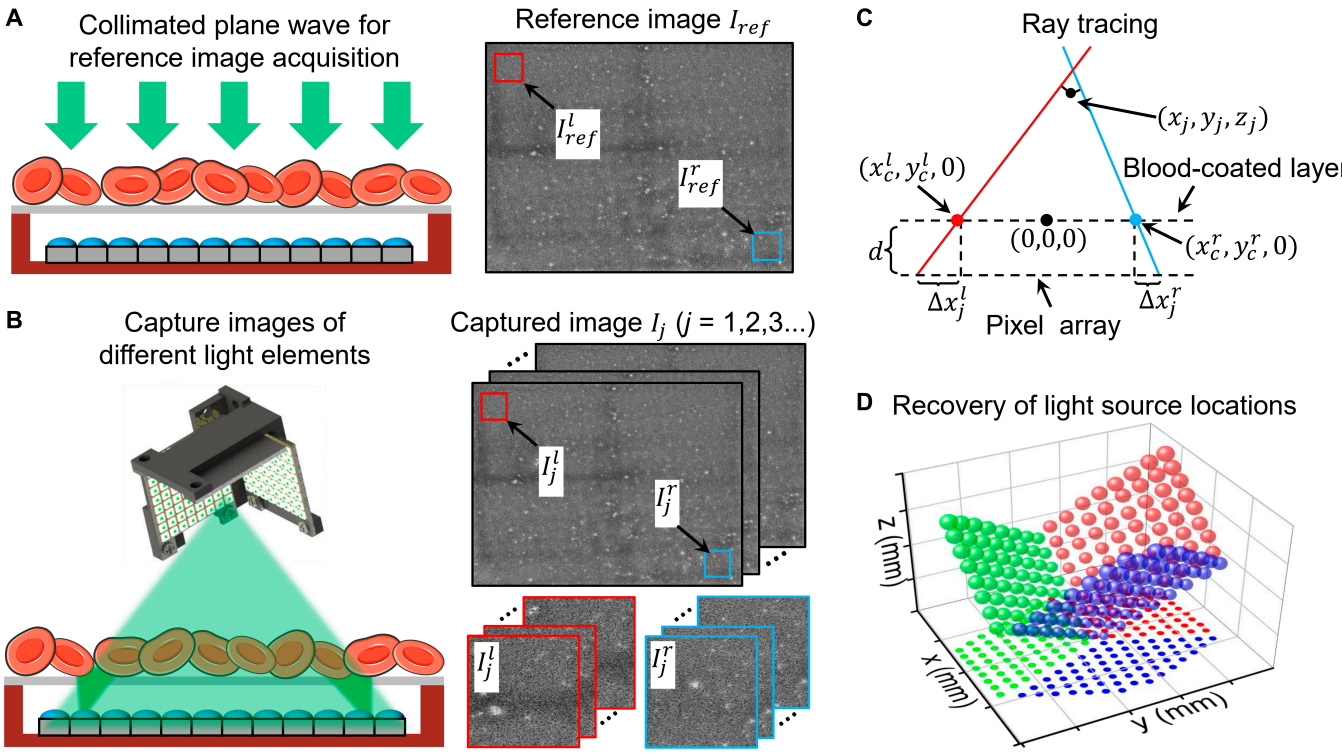

Fig. 3. Recovering the 3D light source positions using the blood-coated image sensor. (A) A reference image I_{ref} is captured under a normal-incidence plane wave. (B) For different light source elements in the freeform illumination, we capture a set of images I_j (j=1, 2, 3...) using the blood-coated sensor. (C) Correlation analysis is performed to recover the positional shifts of the 2 distinct regions of the captured images. The 3D position of the light source can be recovered via a ray tracing process. (D) The positional shifts at 2 distinct regions are used to recover the 3D locations of the light sources, in a way similar to 3D reconstruction via stereo vision.

to the jth light source element of the illuminator, and $\left(\Delta x^r_j, \Delta y^r_j\right)$ represents the positional shift of the right region corresponding to the same element.

In Eqs. 4 and 5, the light waves hitting the 2 regions are treated as 2 collimated plane waves with 2 different angles. Based on the induced positional shifts, we can recover these 2 angles and perform ray tracing to locate the 3D position (x_j, y_j, z_j) of the jth light source element of the illuminator. Assuming the midpoint of the 2 regions is (0, 0) and $z = 0$ for the blood-cell layer plane, we have the following 2 light ray expressions:

$$\text{Left light ray: } \frac{x - x^l_c}{\Delta x^l_j} = \frac{y - y^l_c}{\Delta y^l_j} = \frac{z}{d} \tag{6}$$

$$\text{Right light ray: } \frac{x - x^r_c}{\Delta x^r_j} = \frac{y - y^r_c}{\Delta y^r_j} = \frac{z}{d}, \tag{7}$$

where $\left(x^l_c, y^l_c\right)$ and $\left(x^r_c, y^r_c\right)$ are the spatial coordinates of the central positions of the left and the right tiles in Fig. 3B (highlighted by the red and blue squares) and d is the distance between the blood-coded layer and the pixel array. The format of Eqs. 6 and 7 is also termed "symmetric form" of a line defined in 3D space. As shown in Fig. 3C, the 3D position (x_j, y_j, z_j) of the jth light source element can be recovered by finding a point that is closest to the 2 light rays defined by Eqs. 6 and 7:

$$\left\{x_j, y_j, z_j\right\} = \arg\min_{x_j, y_j, z_j} \left\{ \left| d^l_j\left(x_j, y_j, z_j\right) \right|^2 + \left| d^r_j\left(x_j, y_j, z_j\right) \right|^2 \right\}, \tag{8}$$

where d^l_j denotes the distance between the jth light source element and the left light ray, and d^r_j indicates the distance between the light source element and the right light ray. The expressions of d^l_j and d^r_j can be written as follows:

$$d^r_j = \sqrt{\left(x_j - \left(x^r_c + \Delta x^r_j \cdot t^r_j\right)\right)^2 + \left(y_j - \left(y^r_c + \Delta y^r_j \cdot t^r_j\right)\right)^2 + \left(z_j - d \cdot t^r_j\right)^2}, \tag{9}$$

$$d^l_j = \sqrt{\left(x_j - \left(x^l_c + \Delta x^l_j \cdot t^l_j\right)\right)^2 + \left(y_j - \left(y^l_c + \Delta y^l_j \cdot t^l_j\right)\right)^2 + \left(z_j - d \cdot t^l_j\right)^2} \tag{10}$$

where $t^l_j = \frac{\Delta x^l_j\left(x_j - x^l_c\right) + \Delta y^l_j\left(y_j - y^l_c\right) + d \bullet z_j}{\left(\Delta x^l_j\right)^2 + \left(\Delta y^l_j\right)^2 + (d)^2}$ and $t^r_j = \frac{\Delta x^r_j\left(x_j - x^r_c\right) + \Delta y^r_j\left(y_j - y^r_c\right) + d \bullet z_j}{\left(\Delta x^r_j\right)^2 + \left(\Delta y^r_j\right)^2 + (d)^2}$. If the light source elements all come from a planar surface, we can further fit the recovered positions to a specific 2D surface as follows:

$$\{a, b, c\} = \arg\min_{a,b,c} \sum_j \left| z_j - \left(a + b \cdot x_j + c \cdot y_j\right) \right|^2, \tag{11}$$

where $a + b \bullet x + c \bullet y$ represents a planar surface that contains all light source elements. The z positions can then be updated as $z_j = a + b \bullet x_j + c \bullet y_j$. Figure 3D shows the recovered 3D locations of the light source elements following the above procedures.

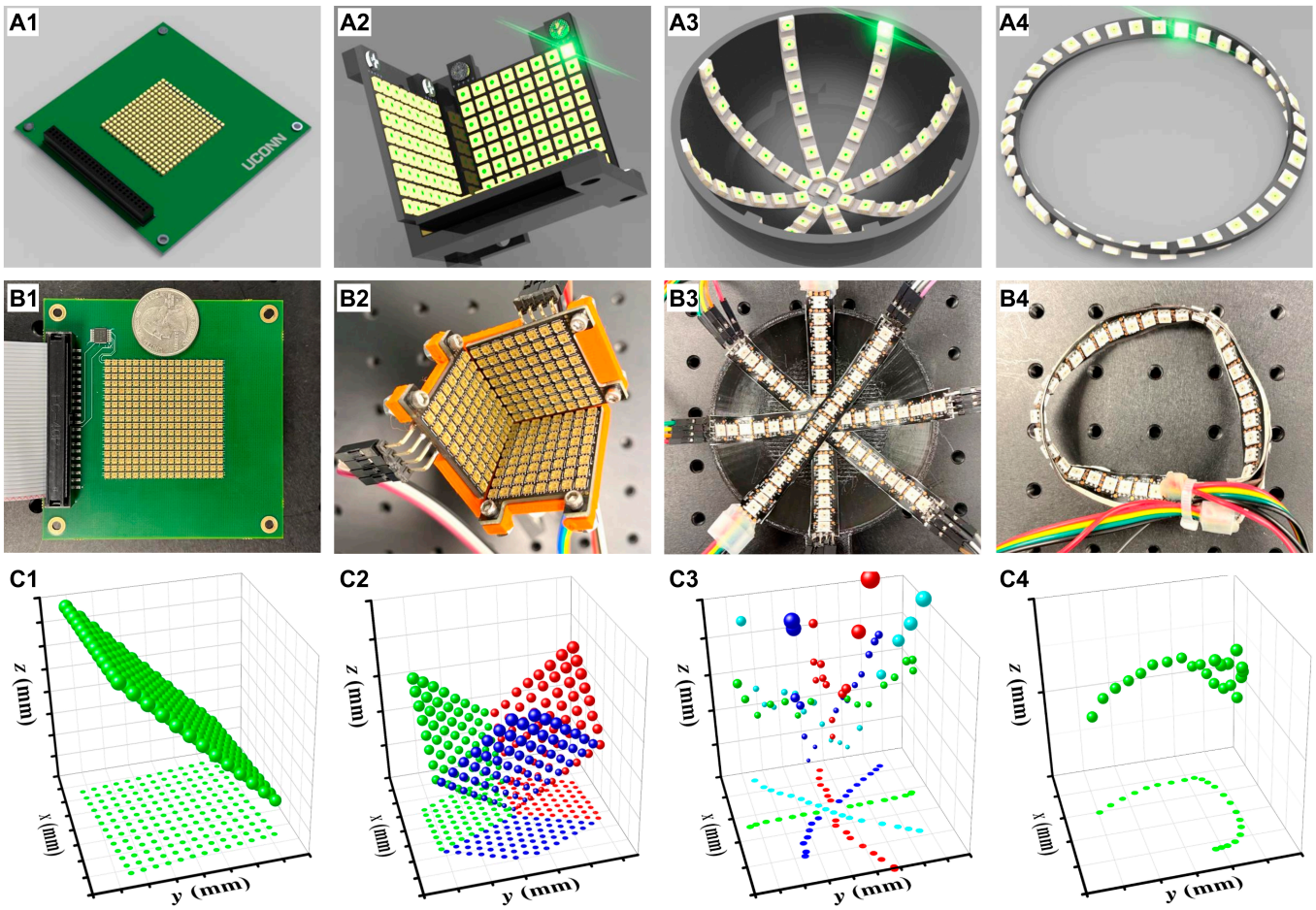

Fig. 4. Design of freeform illuminators and their calibrations using the blood-coated sensor. (A) The design of the freeform illuminators. (B) The prototype devices. (C) The recovery of the 3D light source positions using the blood-coated image sensor.

Results and Discussion

Design of freeform illuminators and their calibrations

Figure 4A shows the design of 4 different freeform illuminators. The first one in Fig. 4A1 is a customized planar LED array built using small-pitch surface mount LEDs (APA102-2020 LED, a pitch of ~2.5 mm) (also refer to the Supplementary Materials). The second one shown in Fig. 4A2 is a design by placing 3 densely packed LED arrays (Adafruit DotStar 3444) on the surfaces of an inverse triangular pyramid. The third one in Fig. 4A3 is a design by placing 4 flexible LED strips on a dome-shaped holder. The fourth one in Fig. 4A4 is 2 LED strips placed at a Mobius band. Figure 4B shows our prototype illuminators. Figure 4C shows the recovered 3D positions of the light sources using the blood-coated image sensor. We note that the planar illuminator in Fig. 4C1 is tilted with a small angle to demonstrate the 3D position recovery capability. We also note that the light from some LED elements of the Mobius illuminator in Fig. 4C4 cannot reach the blood-coated sensor.

We have tested the accuracy of the calibration scheme using the planar illuminator in Fig. 4B1. In this validation experiment, we first aligned the planar illuminator in parallel with the sample plane using a level. We then recovered the 3D positions of the light sources using the calibration procedure discussed above. These recovered 3D positions are compared with the ground-truth positions obtained from the design file of the planar LED array. The standard deviations between the recovered positions and the ground-truth designs are 0.12 mm for the x position, 0.13 mm for the y position, and 0.55 mm for the z position. Given the size of the light source element, these small deviations validate the effectiveness of the proposed calibration process. In the current implementation, we only use 2 small regions for correlation analysis. To further improve the accuracy, we can better model the light source as a point source and use the entire captured images for correlation analysis. With the initial positions obtained from the proposed method, we can further refine them in the reconstruction process, like the position correction schemes employed in the real-space ptychography and FPM [49–52].

Demonstrations in computational microscopy techniques

In the first demonstration, we adopted the freeform illuminators for FPM experiments. The resolution of an FPM platform is determined by $\lambda/(NA_{obj} + NA_{illumination})$, where λ is the wavelength of the LED, NA_{obj} represents the NA of the objective lens, and $NA_{illumination}$ represents the equivalent NA provided by the maximum illumination angle. Figure 5A1 to D1 shows the captured raw images using the 4 freeform illuminators discussed in Fig. 4. The recovered intensity images are shown in Fig. 5A2

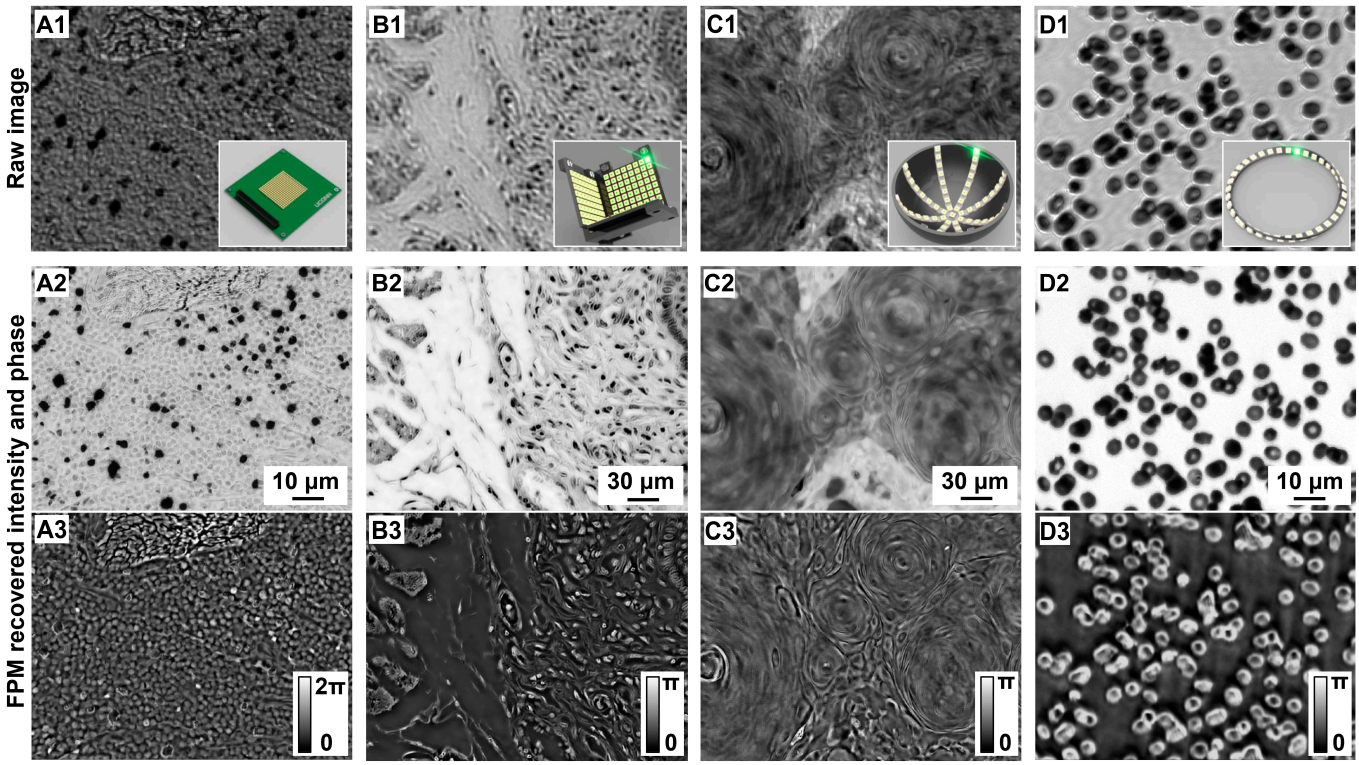

Fig. 5. Freeform illuminator for FPM. (A1 to D1) The captured raw images using 4 different illuminators. (A2 to D2) The recovered intensity image using FPM. (A3 to D3) The recovered phase images using FPM. For (A) and (B), we used a 2×, 0.1 NA objective lens for image acquisition and the maximum synthetic NA is ~0.6. For (C) and (D), we used a 10×, 0.4 NA for image acquisition and the maximum synthetic NA is ~0.7.

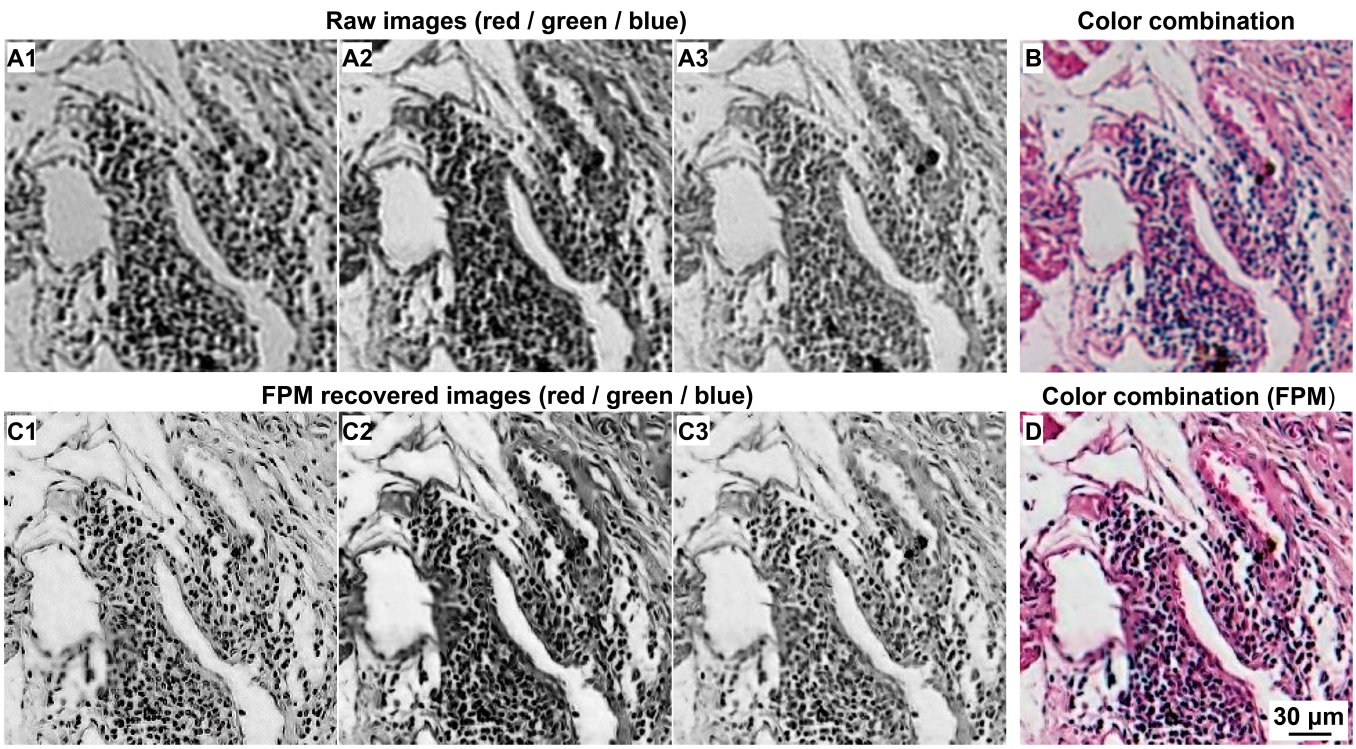

Fig. 6. Color FPM imaging using the pyramid illuminator. (A1 to A3) The captured raw images of pathology slide using the 2×, 0.1 NA objective lens. (B) The combined color image. (C1 to C3) The FPM recovered intensity images with a maximum synthetic NA of ~0.6. (D) The FPM recovered color image.

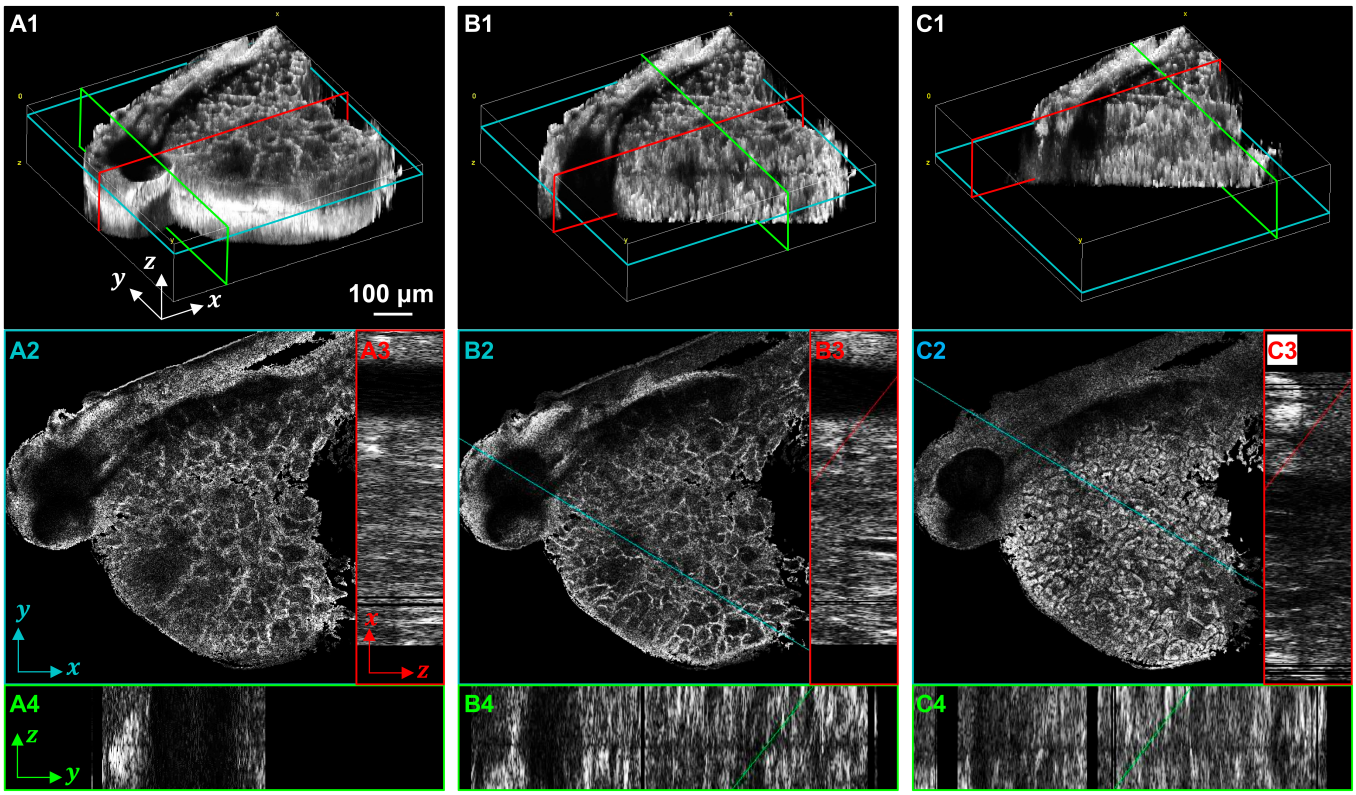

Fig. 7. 3D tomographic imaging using the pyramid illuminator. (A1) The recovered volume of the zebrafish embryo. (A2 to A4) Different cut-through views of the embryo sample. (B and C) Additional views of the recovered volume.

to D2, and the recovered phase images are shown in Fig. 5A3 to D3. For the FPM experiments in Fig. 5A and B, we used a 2×, 0.1 NA objective lens for image acquisition and the maximum synthetic NA is ~0.6. For the experiments in Fig. 5C and D, we used a 10×, 0.4 NA objective lens for image acquisition and the maximum synthetic NA is ~0.7. A higher-NA objective lens can also be used with higher-illumination NA for pushing the resolution limit in the visible light regime [9,21,30,53].

Among different illuminators, there are several advantages of the pyramid illuminator shown in Fig. 5B1. First, the LED elements are angled towards the sample for illumination with a higher optical flux. Second, the distances between different LED elements and the sample vary. The longest distance is for the surface intersection region. As a result, the angular increment is smaller for this region, enabling a denser FPM sampling pattern in the low-frequency region. Since most energy of the sample spectrum is concentrated in this low-frequency region, a higher sampling density enables better convergence for the ptychographic phase retrieval process [54]. Third, the illuminator is built with high-brightness LED elements with a small pitch of 2.5 mm (40% denser compared to the common planar illuminator used in FPM [7]). Therefore, it can be placed closer to the sample to improve the light delivery efficiency. We also note that we did not use all elements in this pyramid illuminator for FPM imaging. In our implementation, we first use elements with illumination NA < 0.1 for image acquisition. We then skip every other element for illumination NA at the range between 0.1 and 0.3. For illumination NA larger than 0.3, we skip every 2 elements to further reduce the data redundancy. The total number of raw images we captured was 76 in this demonstration. Multiplexed illumination and other sampling schemes can be adopted to further reduce the number of acquisitions [8,15,17].

In Fig. 6, we also demonstrate the use of the pyramid illuminator for color FPM imaging. Figure 6A1 to A3 shows the captured raw images using red, green, and blue LEDs from the illuminator. Figure 6B shows the combined color image captured via the 0.1 NA objective lens. Figure 6C1 to C3 shows the FPM recovered intensity images with a synthetic NA of 0.6 and the color combination is shown in Fig. 6D. The freeform illuminator adds flexibility to the system design. One can adopt light sources at different wavelengths for performing multispectral microscopy imaging [55].

In the second demonstration, we adopted the pyramid illuminator for 3D tomographic imaging. In this experiment, we used the 10×, 0.4 NA objective lens for image acquisition. For the illuminator, we skipped every 2 elements to capture one image and the total number of acquisitions is 64. The captured dataset was then used to recover the z-stack of the sample following the filtered back projection algorithm. Figure 7 shows the recovered 3D volume of a zebrafish embryo. Different cut-through views of the volume are shown in Fig. 7A1 to C1. The x–y views, x–z views, and y–z views are also provided in Fig. 7A2 to C2, Fig. 7A3 to C3, and Fig. 7A4 to C4, respectively.

In the current 3D tomographic implementation, we only use bright-field images for performing filtered back projection reconstruction. The lateral resolution is determined by $\lambda/(2NA_{obj})$ and the axial resolution is inversely proportional to NA_{obj}^2. However, it is possible to integrate the concept of FPM into the 3D reconstruction process for improving resolution beyond

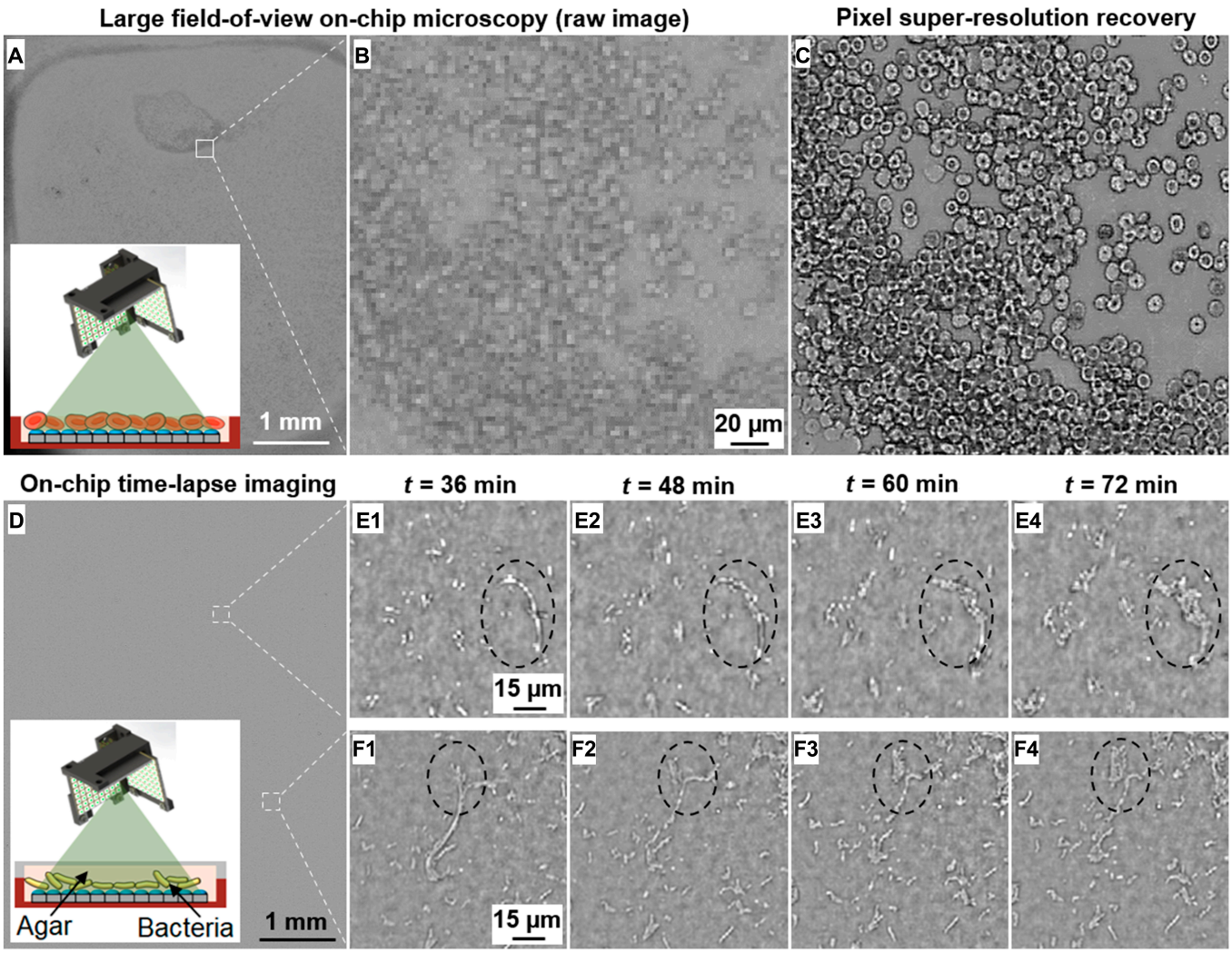

Fig. 8. On-chip microscopy imaging using the pyramid illuminator. (A) The captured large field-of-view image of the blood cells. (B) The zoomed-in view of (A). (C) The recovered super-resolution image of (B). (D) Large field-of-view imaging of live bacterial culture on a chip. (E and F) The time-lapse monitoring of the bacterial growth of 2 zoomed-in regions.

the limit imposed by the objective lens [28]. In this case, both bright-field and dark-field measurements are needed for the ptychographic phase retrieval process and the 3D sample can be modeled using the Ewald sphere in the Fourier space [22]. Tilting the illumination angle will rotate the Ewald sphere around the origin. As such, each captured image corresponds to a spherical cap of the Ewald sphere. Stitching these spherical caps leads to the recovery of the 3D object volume.

In the third demonstration, we used the pyramid illuminator for on-chip microscopy imaging. We removed both the cover-glass and the microlens layer of the sensor so that the sample can be directly placed on top of the pixel array. We first placed a drop of blood on the sensor and captured 64 raw images by tuning on different elements on the pyramid illuminator (skip every 2 elements to capture one image). Figure 8A shows one captured raw image with a large field of view (~6 mm by ~4 mm). Figure 8B shows the zoomed-in view of a small region of Fig. 8A, where we cannot resolve the blood cells placed on the sensor chip. Based on all captured images, we then recover the object image using the pixel super-resolution algorithm [4]. As shown in Fig. 8C, we can clearly resolve the cell details from the reconstruction. For the on-chip microscopy imaging, the lateral resolution is determined by the point spread function of the pixel-sensitive area. It has been shown that submicron resolution can be achieved with adequate angle-varied sampling [4,6,13].

In the second experiment for on-chip microscopy imaging, we used the same pyramid illuminator for time-lapse monitoring of live bacterial culture over a large field of view. The sample preparation procedure can be described as follows. First, we inoculated a single colony of *Escherichia coli* ATCC 25922 strain from the Mueller–Hinton agar plate to 10 ml of fresh Mueller–Hinton broth. Second, we incubated the broth in a culture tube at 37 °C overnight. Third, we adjusted the turbidity of the bacterial solution to 0.5 McFarland standard with fresh Mueller–Hinton medium on the following day. The bacteria suspension was then diluted to a concentration of $\sim 10^3$ CFU/ml. The concentration of the diluted suspension was also checked using the standard plate count method. Lastly, we added the prepared bacteria suspension to a regular Petri dish with Mueller–Hinton agar. We then cut a small block of the agar and placed it on the image sensor. As shown in the inset of Fig. 8D, the bacterial cells directly face the pixel array of the image sensor, thus minimizing the gap between the cells and the active

detection region [13]. Figure 8D shows the recovered super-resolution image of the bacterial culture over a large field of view. Figure 8E and F shows the recovered time-lapse images of 2 zoomed-in views of Fig. 8D. From these zoomed-in views, we can clearly observe the growth of the bacteria cultures. One can further quantify the growth rate by calculating the area occupied by the bacterial cells. Compared to the regular cell monitoring platforms, this chip-scale device with the freeform illuminator has a small footprint and can be directly placed within an incubator. Since the cells directly face the pixel array, the sample focusing issue in conventional imaging systems is no longer a problem for this portable platform. The device can also be integrated with other lab-on-a-chip designs for various imaging and screening applications [56,57].

Conclusion

In summary, we have discussed the development of freeform illuminators that can be arranged at arbitrary 2D or 3D surface structures for computational microscopy. A calibration process has been reported for recovering the 3D positions of different light source elements. The key innovation of this process is the use of a blood-coated image sensor for modulating the incoming light waves from different light source elements. By tracking the positional shift of the blood-cell diffraction patterns at 2 distinct regions, we demonstrated the precise reconstruction of the light source positions in 3D. With the calibrated freeform illuminators, we have discussed their applications in FPM, 3D tomographic imaging, and super-resolution on-chip microscopy. In particular, the small footprint of the proposed pyramid illuminator allows it to be placed closer to the sample with higher optical flux and higher light delivering efficiency. The small angular increment at the low-frequency regime also facilitates better Fourier space sampling in FPM. For on-chip microscopy, we have demonstrated a longitudinal experiment by tracking the bacterial growth over a large field of view. The reported freeform illuminators and the related calibration process offer flexibilities and extended scope for imaging innovations in computational microscopy.

There are several future directions for the reported freeform illuminator. First, the current calibration process only uses 2 small regions of the blood-coated sensor for ray tracing. A better strategy may be to model the light as a point source with spherical waves emitting and recover the wavefront on the blood-coated layer via phase retrieval. Second, we envision that the freeform illuminator can be used for spatial domain coded ptychography [46]. Instead of translating the sample using a mechanical stage, the freeform illuminator can introduce phase diversity with different plane waves. Effort along this line is ongoing. Third, light source elements can also be arranged on a 3D grid with higher spatial density and a smaller footprint. Fourth, light source elements at different wavelengths, from deep ultraviolet to near infrared, can be integrated into the freeform illuminator for multispectral imaging. Lastly, the position estimate process of different light source elements can be affected by many factors such as noise, pixel size of the detector, object, and other system parameters. Further investigation along this line is highly desired.

Acknowledgments

P.S. acknowledges the support of the Thermo Fisher Scientific fellowship. The authors acknowledge the useful discussion with Dr. Zichao Bian. **Funding**: This work was partially supported by the UConn SPARK grant and the National Science Foundation (2012140). **Author contributions**: G.Z. conceived the idea and designed the experiments. P.S. and T.W. conducted the experiments. All authors contributed equally to the writing and revision of the manuscript. **Competing interests**: The authors declare that they have no competing interests.

Data Availability

The calibration code for the freeform illuminator is available from the corresponding author upon reasonable request.

References

1. Sanchez C, Cristóbal G, Bueno G, Blanco S, Borrego-Ramos M, Olenici A, Pedraza A, Ruiz-Santaquiteria J. Oblique illumination in microscopy: A quantitative evaluation. *Micron*. 2018;105:47–54.
2. Isikman SO, Bishara W, Mavandadi S, Yu FW, Feng S, Lau R, Ozcan A. Lens-free optical tomographic microscope with a large imaging volume on a chip. *Proc Natl Acad Sci USA*. 2011;108:7296–7301.
3. Isikman SO, Bishara W, Sikora U, Yaglidere O, Yeah J, Ozcan A. Field-portable lensfree tomographic microscope. *Lab Chip*. 2011;11:2222–2230.
4. Zheng G, Lee SA, Antebi Y, Elowitz MB, Yang C. The ePetri dish, an on-chip cell imaging platform based on subpixel perspective sweeping microscopy (SPSM). *Proc Natl Acad Sci USA*. 2011;108:16889–16894.
5. Zheng G, Kolner C, Yang C. Microscopy refocusing and dark-field imaging by using a simple LED array. *Opt Lett*. 2011;36:3987–3989.
6. Lee SA, Zheng G, Mukherjee N, Yang C. On-chip continuous monitoring of motile microorganisms on an ePetri platform. *Lab Chip*. 2012;12:2385–2390.
7. Zheng G, Horstmeyer R, Yang C. Wide-field, high-resolution Fourier ptychographic microscopy. *Nat Photonics*. 2013;7:739–745.
8. Tian L, Li X, Ramchandran K, Waller L. Multiplexed coded illumination for Fourier ptychography with an LED array microscope. *Biomed Opt Express*. 2014;5:2376–2389.
9. Ou X, Horstmeyer R, Zheng G, Yang C. High numerical aperture Fourier ptychography: Principle, implementation and characterization. *Opt Express*. 2015;23:3472–3491.
10. Tian L, Liu Z, Yeh L-H, Chen M, Zhong J, Waller L. Computational illumination for high-speed in vitro Fourier ptychographic microscopy. *Optica*. 2015;2:904–911.
11. Phillips ZF, D'Ambrosio MV, Tian L, Rulison JJ, Patel HS, Sadras N, Gande AV, Switz NA, Fletcher DA, Waller L. Multi-contrast imaging and digital refocusing on a mobile microscope with a domed led array. *PLOS ONE*. 2015;10(5):e0124938.
12. Tian L, Waller L. 3D intensity and phase imaging from light field measurements in an LED array microscope. *Optica*. 2015;2:104–111.
13. Jung JH, Lee JE. Real-time bacterial microcolony counting using on-chip microscopy. *Sci Rep*. 2016;6:1–8.
14. Jung D, Choi J-H, Kim S, Ryu S, Lee W, Lee J-S, Joo C. Smartphone-based multi-contrast microscope using color-multiplexed illumination. *Sci Rep*. 2017;7:1–10.
15. Sun J, Zuo C, Zhang J, Fan Y, Chen Q. High-speed Fourier ptychographic microscopy based on programmable annular illuminations. *Sci Rep*. 2018;8:1–12.

16. Pan A, Zhang Y, Wen K, Zhou M, Min J, Lei M, Yao B. Subwavelength resolution Fourier ptychography with hemispherical digital condensers. *Opt Express*. 2018;26:23119–23131.
17. Lee W, Choi J-H, Ryu S, Jung D, Song J, Lee J-S, Joo C. Color-coded LED microscopy for quantitative phase imaging: Implementation and application to sperm motility analysis. *Methods*. 2018;136:66–74.
18. Zhang Z, Zhou Y, Jiang S, Guo K, Hoshino K, Zhong J, Suo J, Dai Q, Zheng G. Invited Article: Mask-modulated lensless imaging with multi-angle illuminations. *APL Photonics*. 2018;3:060803.
19. Zhou Y, Wu J, Suo J, Han X, Zheng G, Dai Q. Single-shot lensless imaging via simultaneous multi-angle LED illumination. *Opt Express*. 2018;26:21418–21432.
20. Zhang H, Bian Z, Jiang S, Liu J, Song P, Zheng G. Field-portable quantitative lensless microscopy based on translated speckle illumination and sub-sampled ptychographic phase retrieval. *Opt Lett*. 2019;44:1976–1979.
21. Lee H, Chon BH, Ahn HK. Reflective Fourier ptychographic microscopy using a parabolic mirror. *Opt Express*. 2019;27:34382–34391.
22. Zuo C, Sun J, Li J, Asundi A, Chen Q. Wide-field high-resolution 3D microscopy with Fourier ptychographic diffraction tomography. *Opt Lasers Eng*. 2020;128:106003.
23. Lee KC, Lee K, Jung J, Lee SH, Kim D, Lee SA. A smartphone-based fourier ptychographic microscope using the display screen for illumination. *ACS Photonics*. 2021;8:1307–1315.
24. Guo C, Bian Z, Jiang S, Murphy M, Zhu J, Wang R, Song P, Shao X, Zhang Y, Zheng G. OpenWSI: A low-cost, high-throughput whole slide imaging system via single-frame autofocusing and open-source hardware. *Opt Lett*. 2020;45:260–263.
25. Chung J, Lu H, Ou X, Zhou H, Yang C. Wide-field Fourier ptychographic microscopy using laser illumination source. *Biomed Opt Express*. 2016;7:4787–4802.
26. Luo W, Greenbaum A, Zhang Y, Ozcan A. Synthetic aperture-based on-chip microscopy. *Light Sci Appl*. 2015;4:e261.
27. Li P, Maiden A. Lensless LED matrix ptychographic microscope: Problems and solutions. *Appl Opt*. 2018;57:1800–1806.
28. Horstmeyer R, Chung J, Ou X, Zheng G, Yang C. Diffraction tomography with Fourier ptychography. *Optica*. 2016;3:827–835.
29. Chan AC, Kim J, Pan A, Xu H, Nojima D, Hale C, Wang S, Yang C. Parallel Fourier ptychographic microscopy for high-throughput screening with 96 cameras (96 eyes). *Sci Rep*. 2019;9(1):11114.
30. Sun J, Zuo C, Zhang L, Chen Q. Resolution-enhanced Fourier ptychographic microscopy based on high-numerical-aperture illuminations. *Sci Rep*. 2017;7(1):1187.
31. Li J, Chen Q, Zhang J, Zhang Z, Zhang Y, Zuo C. Optical diffraction tomography microscopy with transport of intensity equation using a light-emitting diode array. *Opt Lasers Eng*. 2017;95:26–34.
32. Salvador-Balaguer E, Latorre-Carmona P, Chabert C, Pla F, Lancis J, Tajahuerce E. Low-cost single-pixel 3D imaging by using an LED array. *Opt Express*. 2018;26:15623–15631.
33. Zuo C, Sun J, Zhang J, Hu Y, Chen Q. Lensless phase microscopy and diffraction tomography with multi-angle and multi-wavelength illuminations using a LED matrix. *Opt Express*. 2015;23:14314–14328.
34. Wu X, Zhao J, Cui G, Mao H. A lensless LED matrix-based ptychographic microscopy imaging method using loss correction and adaptive step size. *Opt Lasers Eng*. 2022;152:106980.
35. Song S, Kim J, Hur S, Song J, Joo C. Large-area, high-resolution birefringence imaging with polarization-sensitive Fourier ptychographic microscopy. *ACS Photonics*. 2021;8:158–165.
36. Tian L, Waller L. Quantitative differential phase contrast imaging in an LED array microscope. *Opt Express*. 2015;23:11394–11403.
37. Baek Y, Park Y. Intensity-based holographic imaging via space-domain Kramers–Kronig relations. *Nat Photonics*. 2021;15:354–360.
38. Guo K, Dong S, Zheng G. Fourier ptychography for brightfield, phase, darkfield, reflective, multi-slice, and fluorescence imaging. *IEEE J Sel Top Quantum Electron*. 2015;22:6802712.
39. Guo Y, Guo R, Qi P, Zhou Y, Zhang Z, Zheng G, Zhong J. Robust multi-angle structured illumination lensless microscopy via illumination angle calibration. *Opt Lett*. 2022;47:1847–1850.
40. Sun J, Chen Q, Zhang J, Fan Y, Zuo C. Single-shot quantitative phase microscopy based on color-multiplexed Fourier ptychography. *Opt Lett*. 2018;43:3365–3368.
41. Farsiu S, Robinson MD, Elad M, Milanfar P. Fast and robust multiframe super resolution. *IEEE Trans Image Process*. 2004;13:1327–1344.
42. Zheng G, Shen C, Jiang S, Song P, Yang C. Concept, implementations and applications of Fourier ptychography. *Nat Rev Phys*. 2021;3:207–223.
43. Li P, Batey DJ, Edo TB, Rodenburg JM. Separation of three-dimensional scattering effects in tilt-series Fourier ptychography. *Ultramicroscopy*. 2015;158:1–7.
44. Shen C, Liang M, Pan A, Yang C. Non-iterative complex wave-field reconstruction based on Kramers–Kronig relations. *Photonics Res*. 2021;9:1003–1012.
45. Maiden AM, Rodenburg JM. An improved ptychographical phase retrieval algorithm for diffractive imaging. *Ultramicroscopy*. 2009;109:1256–1262.
46. Jiang S, Guo C, Song P, Zhou N, Bian Z, Zhu J, Wang R, Dong P, Zhang Z, Liao J, et al. Resolution-enhanced parallel coded ptychography for high-throughput optical imaging. *ACS Photonics*. 2021;8:3261–3271.
47. Popoff SM, Lerosey G, Carminati R, Fink M, Boccara AC, Gigan S. Measuring the transmission matrix in optics: An approach to the study and control of light propagation in disordered media. *Phys Rev Lett*. 2010;104:100601.
48. Jiang S, Guo C, Wang T, Liu J, Song P, Zhang T, Wang R, Feng B, Zheng G. Blood-coated sensor for high-throughput ptychographic cytometry on a Blu-ray disc. *ACS Sens*. 2022;7:1058–1067.
49. Maiden A, Humphry M, Sarahan M, Kraus B, Rodenburg J. An annealing algorithm to correct positioning errors in ptychography. *Ultramicroscopy*. 2012;120:64–72.
50. Zhang F, Peterson I, Vila-Comamala J, Diaz A, Berenguer F, Bean R, Chen B, Menzel A, Robinson IK, Rodenburg JM. Translation position determination in ptychographic coherent diffraction imaging. *Opt Express*. 2013;21:13592–13606.
51. Bian L, Zheng G, Guo K, Suo J, Yang C, Chen F, Dai Q. Motion-corrected Fourier ptychography. *Biomed Opt Express*. 2016;7:4543–4553.
52. Eckert R, Phillips ZF, Waller L. Efficient illumination angle self-calibration in Fourier ptychography. *Appl Opt*. 2018;57:5434–5442.
53. Liang M, Yang C. Implementation of free-space Fourier ptychography with near maximum system numerical aperture. *Opt Express*. 2022;30:20321–20332.

54. Guo K, Dong S, Nanda P, Zheng G. Optimization of sampling pattern and the design of Fourier ptychographic illuminator. *Opt Express*. 2015;23:6171–6180.
55. Hoshino K, Joshi PP, Bhave G, Sokolov KV, Zhang X. Use of colloidal quantum dots as a digitally switched swept light source for gold nanoparticle based hyperspectral microscopy. *Biomed Opt Express*. 2014;5: 1610–1615.
56. Clausell-Tormos J, Lieber D, Baret J-C, El-Harrak A, Miller OJ, Frenz L, Blouwolff J, Humphry KJ, Köster S, Duan H. Droplet-based microfluidic platforms for the encapsulation and screening of mammalian cells and multicellular organisms. *Chem Biol*. 2008;15:427–437.
57. Crane MM, Chung K, Stirman J, Lu H. Microfluidics-enabled phenotyping, imaging, and screening of multicellular organisms. *Lab Chip*. 2010;10:1509–1517.